Different ionization mechanisms in pulsed micro-DBD's in argon at different pressures

Yaogong Wang[1,2,*] ⓘ**, Xiaoqin Ma**[1,2]ⓘ**, Dennis Bouwman**[3]ⓘ**,**
Zhuoran Liu[1,2]**, Ute Ebert**[3,4]ⓘ **and Xiaoning Zhang**[1,2]

[1] Key Laboratory of Physical Electronics and Devices of the Ministry of Education,
Xi'an Jiaotong University, Xi'an, Shaanxi, People's Republic of China
[2] School of Electronic Science and Engineering, Xi'an Jiaotong University, Xi'an, Shaanxi, 710049,
People's Republic of China
[3] Centrum Wiskunde & Informatica, PO Box 94079, 1090 GB Amsterdam, The Netherlands
[4] Department of Applied Physics, Eindhoven University of Technology, PO Box 513, 5600 MB
Eindhoven, The Netherlands

E-mail: wyg008@xjtu.edu.cn

CrossMark

Abstract
In this research we analyse different plasma wave propagation mechanism of microcavity discharge in pure argon at two different pressures. Experimental results of a pulsed micro-DBD with 2 and 50 kPa argon, 180 μm gap, at room temperature, show that two distinct pressure-dependent propagation modes exist. In the low pressure regime, the discharge propagates perpendicular to the applied electric field forming distinct channels, but many vertically-oriented filaments distributed throughout the domain at high pressure discharge. And the discharge duration time in high pressure is around 5 times shorter than that in low pressure. A 2D particle-in-cell (PIC-MCC) model with chemical reactions, photoemission, and secondary electron generation, is established to investigate the formation mechanism of the two propagation modes. Models of the initial ionization processes show that there are two different breakdown mechanisms for these two pressures, where secondary emission of electrons from the dielectric is dominated either by ion impact or by photon impact. The investigation is of great significance for further reveal of the principle of microplasmas discharge.

Keywords: microplasma, inception discharge, UV photon, photoemission, secondary electron emission

(Some figures may appear in colour only in the online journal)

1. Introduction

Microplasmas are electric discharges confined to a limited space, usually of the order of micrometers. They show nonlinear behavior such as front propagation, periodic or nonperiodic self-organization, mode transition and so on [1–3]. Microplasmas are of great significance for engineering applications, like surface modification, biomedicine, environmental protection [4–12]. Microplasma properties have been investigated [13–16], and although the discharge conditions, background gas and device structure in these works are not exactly the same as those in this paper, their results and discussions have significantly guided the analysis of our work. Experimental studies can show different macroscopic morphologies of the micro-discharge [17–19], but they cannot easily show how the nonlinear dynamics is determined by microscopic reaction processes.

Numerical simulations based on microscopic mechanisms can elucidate different types of nonlinear dynamics and the

---

* Author to whom any correspondence should be addressed.

corresponding spatial-temporal distributions of particles (like electrons, ions, excited atoms and molecules) and electric fields in the discharge. Various researches show that the simulation is an essential way to investigate the gas discharge evolution process and more details of plasma characteristics can be obtained. It has guiding significance in adjusting the plasma discharge characteristics through manipulation. Liu *et al* [20] used a two-dimensional self-consistent fluid model to investigate the effect of the electrode gap on the plasma properties-electron density and electron temperature-in Ar discharge, and they ascribed the results to a mode transition from the γ regime to the α regime. Akishev [21] *et al* carried out a numerical calculation and indicated that, in the steady-state DBD, the volume plasma is responsible for the existence of micro-discharge spatial 'memory' and the deposited surface charge is responsible for micro-discharge jittering in time. Seo [22] *et al* utilized a two-dimensional fluid simulation of microplasma to investigate the temporal history of the spatially resolved electron and ion number densities in response to an ac-driven voltage waveform, and discovered the dependence of plasma development on the *pd* values. Lee [23] *et al* calculated the particle densities and energy flow in the microcavities with parabolic sidewalls that fabricated in nanoporous alumina. Some simulation works [24–28] have been carried out to investigate the mechanism of ionization wave propagation, however, few simulations are reported to investigate the ionization wave propagation in micro-discharge, especially at different circumstances, such as pressure dependent.

Considering our previous work, in which the device structure is the same as that in this paper, self-organization of periodic ionization waves originated from a single point but rapidly sub-divide into as many as 10 'branch' plasma wave packets that eventually recombine have been observed. These filaments propagate perpendicular to the electric field [29]. However, in reference [29], the formation mechanism of these plasma branches is intuitively analyzed, and the results are only investigated under low pressure circumstance. Since new electrons from electron impact or photon ionization, and secondary electron generation from surfaces, including photoemission, are critical in discharge evolution, and these new electron supplement reactions are number density dependent, experimental combined with numerical study are proposed to get insight into the mechanism of discharge inception and ionization wave propagation under different pressure. The details of secondary electron generation mechanism, and local vs nonlocal phenomena at different pressures are discussed.

The rest part of this article is organized as follows: section 2 describes the experimental apparatus and results. The different microscopic processes in a micro-DBD in argon are presented in section 3. Section 4 exhibits the implementation and solution of a PIC-MCC model for the discharges. The simulation results at different pressures and discussions are displayed in section 5. Finally, some concluding remarks are summarized in section 6.

2. Experimental setup and results

2.1. Experimental setup and data acquisition

In this work we investigate microdischarges in a dielectric barrier discharge (DBD) configuration where the gas discharge is confined to a volume with dimensions of 10 mm × 10 mm × 180 μm, and the electric field is applied over the short gas gap of 180 μm. The domain, which we refer to as the microcavity, is shown in figure 1, and drawn in modeling detail in figure 5. Conductive silver paste is applied on the backside of a heavily doped n-type Si substrate (0.01 Ω cm < resistivity < 0.02 Ω cm), and the combination of Si and silver serves as the grounded electrode (bottom). A piece of 180 μm polyimide film (Kapton tape) was stuck on the topside of the Si substrate as a barrier and a 10 mm ×10 mm square aperture was carved in the tape to form the discharge space (microcavity). An ITO glass was sealed on top of the microcavity structure, and glass was placed on the tape as a dielectric layer, in order to protect the ITO electrode from bombardment of energetic ions.

In the experiment, the device is connected to a vacuum system through a tube. Firstly, the vacuum system is used to vacuumize the device down to $\sim 10^{-3}$ Pa. Then, the target gas (Argon) is transported into the device through a gas tank. When the pressure reaches the expected value, the inlet tube valve is closed to maintain the device under the settled pressure, which are 2 kPa and 50 kPa in the experiment.

A continuous pulse with 1.6 kV amplitude, 20 kHz frequency, 400 ns rising/falling time and 5 μs pulse duration was applied to the microcavity as shown by the black line in figure 1(b). The electrical signals (voltage and current) generated during the discharge were detected with a high-voltage probe and a current probe, and monitored by an oscilloscope. The current waveform detected in the microdischarge at low pressure 2 kPa is demonstrated by the red line in figure 1(b). An intensified charged coupled device (ICCD) was used to capture optical signals during the discharge.

2.2. Experimental results

To observe the diversity of microdischarge morphologies at different pressures, time-integrated images of microplasma at 1, 2, 3, 5, 7, 10, 13.3, 30 and 50 kPa have been captured by ICCD with 200 ms exposure time, as displayed in figure 2. On these images, distinct discharge channels can be seen at low pressure. But these separate channels (as indicated by the black arrows) are not visible anymore at 13.3 kPa and above, the microplasma is evenly distributed in the microcavity domain.

Here, the temporal evolution of micro discharge at low pressure 2 kPa and high pressure 50 kPa are taken as example to explore the ionization mechanism at different pressures as displayed in figure 3. The gate width of ICCD was fixed at 3 ns, and each frame was a superposition of 4000 discharge cycles. $T = 0$ is defined as the start point of pulse rising edge, and from figure 3(a), the ionization waves originated from the corners near the downside of the cavity at $\sim$595 ns, then separate branches are formed and propagate along the
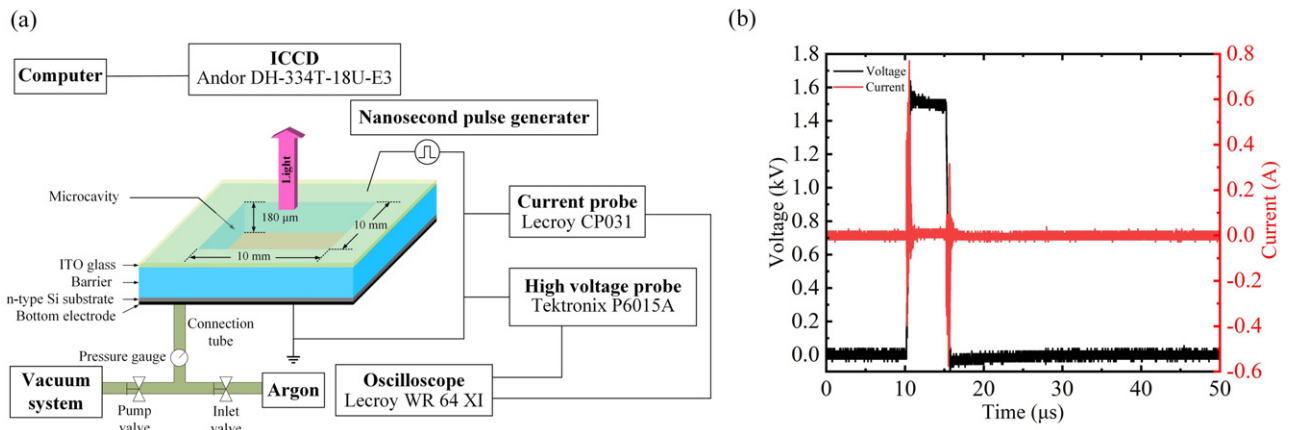
Figure 1. (a) The schematic of device structure and measurement system adopted for the experiments, (b) voltage and current detected in the microdischarge at 2 kPa.
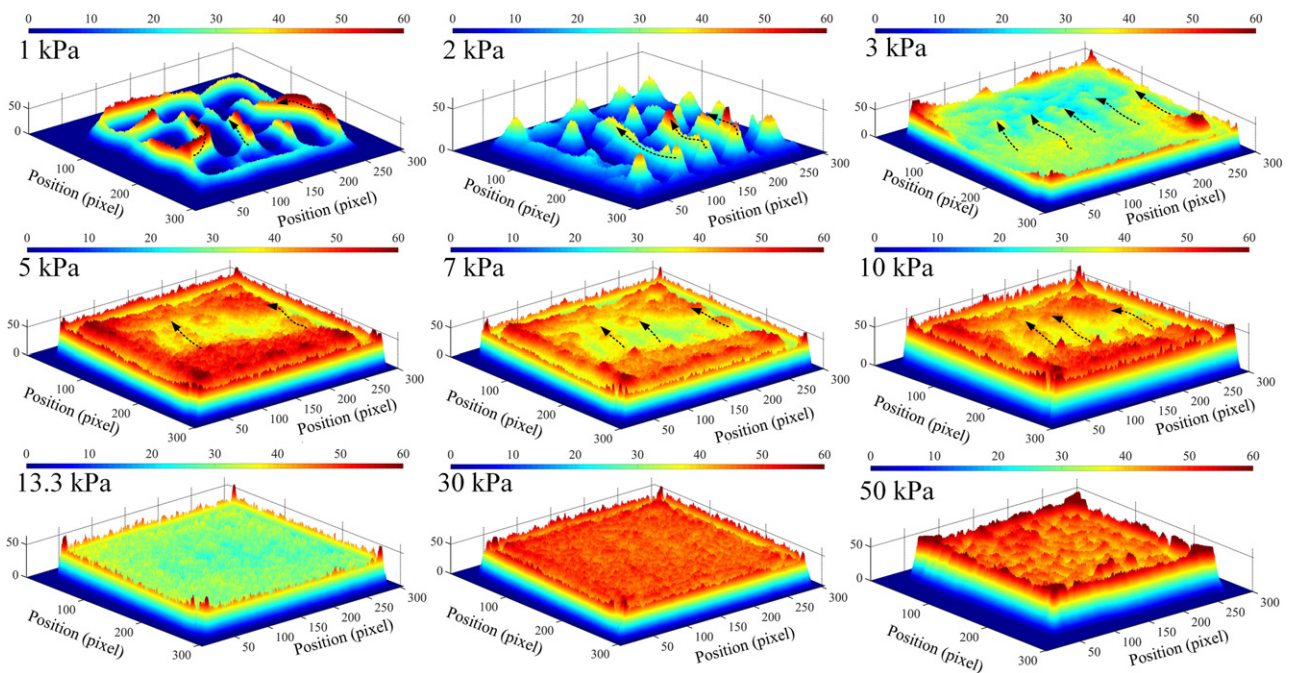

Figure 2. Images of microdischarges at different pressures with 1.6 kV pulses at 20 kHz repetition frequency, integrated over 200 ms.

longitudinal direction to the upside of the cavity at ∼631 ns and ∼673 ns as illustrated in figures 3(a-ii) and (a-iii). At ∼715 ns, the transmission process is completed and the discharge extinguishes at the upper-right corner. Similar results were also reported in reference [29]. However, for high pressure 50 kPa, the discharge emerges in the largest part of the cavity, and the microplasma is rather evenly distributed in the whole region of the cavity after ∼15 ns as presented in figure 3(b). Then, the discharge gradually distinguishes with the same distribution pattern.

So a rather evenly spread microplasma appears at high pressure, and there is a clear ionization wave propagation with

branches at low pressure. The formation mechanism of this phenomenon will be discussed in the following.

To observe the appearance of the discharge during the first voltage pulse, single-shot ICCD images of microplasma evolution at different pressures 2 kPa and 50 kPa have been captured and illustrated in figure 4. To start the discharge, a higher voltage of 6 kV had to be applied. The upper part of figure 4 shows some distinct discharge channels (top view) being formed at 2 kPa; they are perpendicular to the electric field. However, for a pressure of 50 kPa discharge filaments (that we see as bright dots in top view) evenly distributed in the microcavity are obtained.
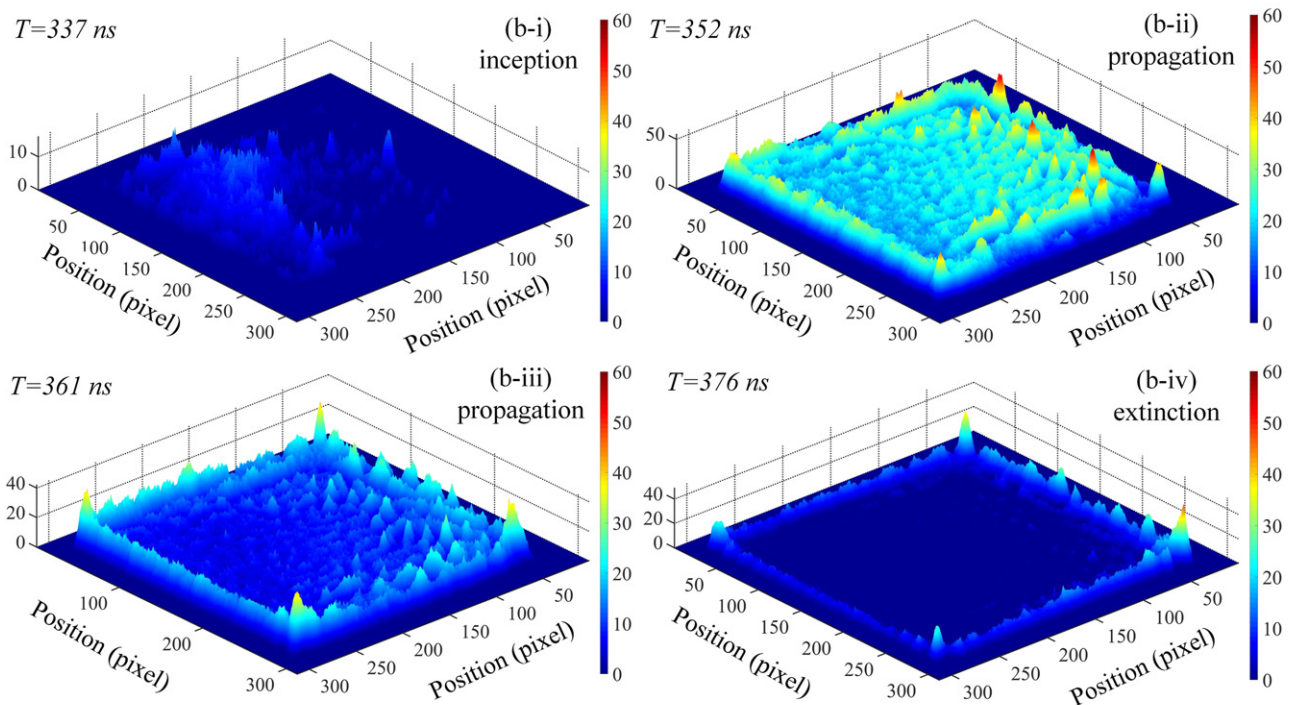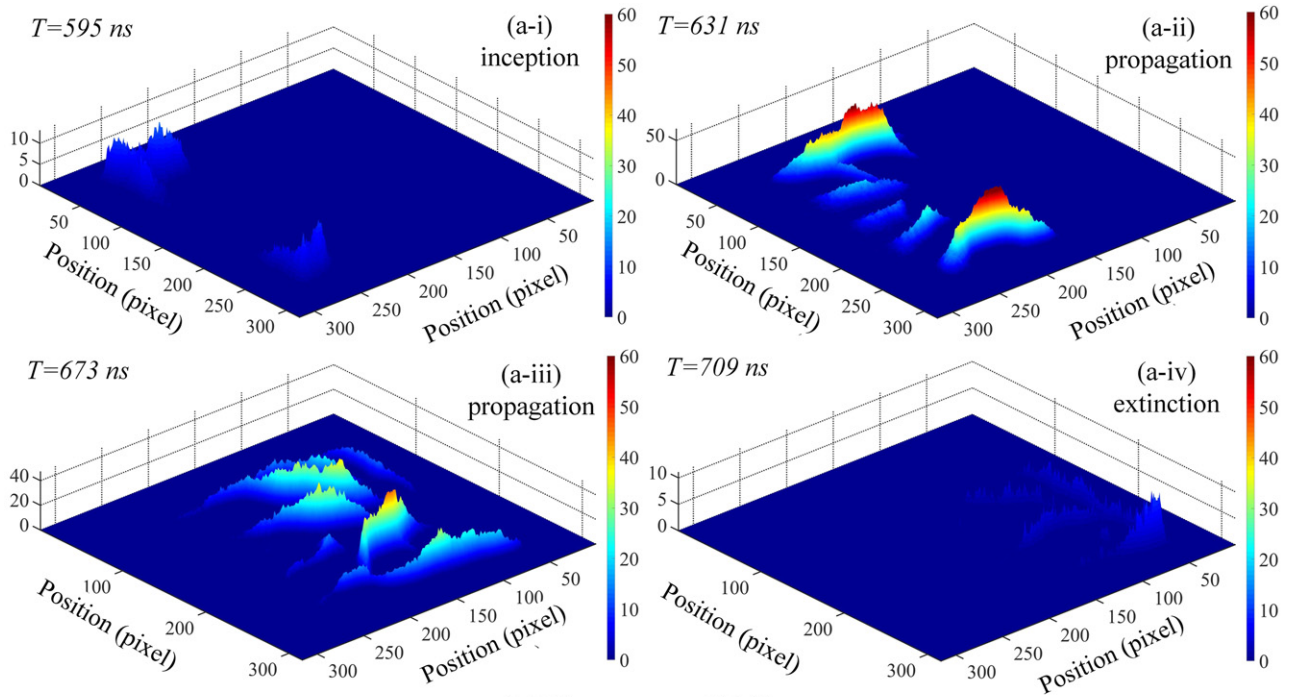
(a) Pressure = 2 kPa

(b) Pressure = 50 kPa

Figure 3. The development of the discharge morphologies within a voltage pulse at different pressures. (a) Low pressure 2 kPa, (b) high pressure 50 kPa. The camera opens at the times indicated ($T = 595$ ns etc) for 3 ns, and the figures are accumulated over 4000 voltage pulses.
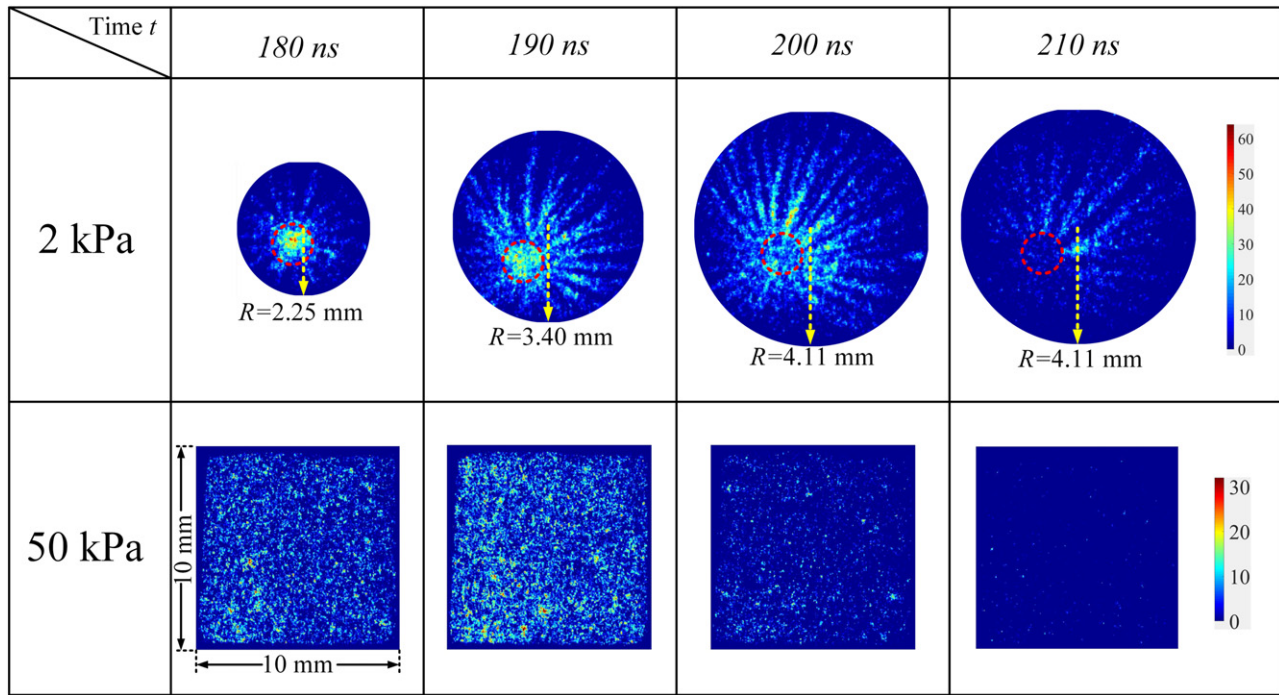
Figure 4. The single-shot ICCD images of microplasma ionization evolution at 2 kPa and 50 kPa. To start these non-repetitive discharges, a higher voltage of 6 kV was applied.

3. Different microscopic processes in micro-DBD in argon

A discharge starts with electrons being liberated by sources like radioactivity or cosmic rays. These electrons are accelerated by the applied electric field, and they lose energy in collisions with gas atoms or molecules and with surfaces. If the field is high enough, the electrons generate ionization avalanches, and an electric discharge starts. Here we first discuss the specific processes in the bulk of the gas and on the surfaces that can be important for a micro-DBD in pure argon. Then we argue which processes are relevant in the two specific experiments introduced above.

3.1. Bulk process

Electron-collisions with neutral gas atoms are treated stochastically and all scattering processes are assumed to be isotropic. The cross sections for the considered collisions are taken from Hayashi's database [30] retrieved from LXCat [31] at August 14 2018. The model established here is simplified and the main reactions are summarized in table 1. Reaction (1) and (2) in table 1 use cross sections data, and the rest are calculated by rate coefficient. The possibility of UV photon absorption by excited argon species, such as photo absorption by Ar^* and Ar_2^*, or photo-dissociation, may be excluded due to their small cross sections that the VUV absorption cross section is in range of 1×10^{-19} cm^2 [38, 39]. Therefore, the photon absorption process is not considered in the model. In addition, the spectral profiles of the Ar_2^* excimers, singlet state $Ar_2^*(^1\sum_u)$ and triplet state $Ar_2^*(^3\sum_u)$, are very close. Since the radiation rate constant from $Ar_2^*(^3\sum_u)$ is 3 orders smaller than

$Ar_2^*(^1\sum_u)$, the $h\nu$ from $Ar_2^*(^3\sum_u)$ is neglected and the UV radiation is mainly emitted from short-lived singlet molecules $Ar_2^*(^1\sum_u)$.

Scaling with pressure: the electrons will be modelled as particles, as discussed below. The ions will be modelled as a density and characterized by a drift velocity which is determined by the electric field and the mobility. The mobility is a function of the reduced electric field E/N, where E is the electric field and the N is the number density of background gas. In this work, a lookup table was created to obtain the ion mobility at different pressures and it is shown in figure 5. At very high reduced electric field (>1000 Td) and low reduced electric field (<1 Td), the ion mobility is acquired referring to [40, 41], and for other reduced electric fields the ion mobility is estimated by an exponential function [42]. In addition, the ion mobility at different pressure is calculated through the scaling relation

$$\mu_{ion} = \mu_{atm} * (N_{atm}/N), \tag{1}$$

where μ_{ion} and N are the ion mobility and number density of the gas at different pressures. μ_{atm} and N_{atm} are the ion mobility and number density of the gas at 1 atm. Figure 5 gives the ion mobility at 2 kPa and 50 kPa, in which the blue and red line stands for the ion mobility at 2 kPa and 50 kPa respectively. From figure 5, the mobility of Ar^+ at 2 kPa can reach to $\sim 10^{-3}$ m^2 Vs^{-1}, and the maximum mobility of Ar^+ at 50 kPa is only $\sim 3.02 \times 10^{-4}$ m^2 Vs^{-1}.

3.2. Surface process

The secondary electron emission stimulated by ions (γ_i), metastable atoms (γ_m) and photons (γ_p) play a key role in DBD. The Townsend ionization coefficient is naturally

Table 1. Reactions included in the model.

| Reactions	Rate coefficient (cm⁶ s⁻¹, cm³ s⁻¹, s⁻¹)	References
2 body reaction with e		
1 e + Ar → Ar⁺ + 2e	[a]Cross sections data	[30]
2 e + Ar → Ar* + e	Cross sections data	[30, 32]
3 e + Ar* → Ar⁺ + 2e	[b]$1 \times 10^{-6} \exp(-4/T_e)$ cm³ s⁻¹	[33]
4 e + Ar* → Ar + e (fast)	3×10^{-10} cm³ s⁻¹	[34]
5 e + Ar₂* → Ar₂⁺ + 2e	$1 \times 10^{-6} \exp(-4/T_e)$ cm³ s⁻¹	[35]
6 e + Ar₂* → Ar* + Ar + e	$1 \times 10^{-8} \exp(-1/T_e)$ cm³ s⁻¹	[34]
7 e + Ar₂*($^3\sum_u$) → Ar₂*($^1\sum_u$) + e	5×10^{-8} cm³ s⁻¹	[34]
3 body reaction with Ar gas		
8 Ar*(4s³P₂) + 2Ar → Ar₂*($^3\sum_u$) + Ar	[c]$1.3 \times 10^{-32} F(n_e/n_a)$ cm⁶ s⁻¹	[34]
9 Ar*(4s³P₁) + 2Ar → Ar₂*($^1\sum_u$) + Ar	$1.5 \times 10^{-33} F(n_e/n_a)$ cm⁶ s⁻¹	[34]
Radiation transition		
10 Ar*(4p) → Ar(1s₅, 1s₄, 1s₃, 1s₂) + hν	1.6×10^7, 9.3×10^6, 3.0×10^6, 8.5×10^6 s⁻¹	[36]
11 [d]Ar*(4d) → Ar(1s₅, 1s₄, 1s₃, 1s₂) + hν	1.8×10^5, 1.2×10^5, 3.7×10^4, 9.3×10^4 s⁻¹	[36]
12 [e]Ar₂*($^1\sum_u$) → 2Ar + hν	2.4×10^8 s⁻¹	[34]
13 Ar(1s4) → Ar + hν	1.2×10^8 s⁻¹	[37]

[a]Cross sections data is from Hayashi Database retrieved from LXCat [31].

[b]T_e is the electron temperature in eV.

[c]Function F is defined as $F = (1 + 30000 n_e/n_a)^{-1}$, n_e and n_a are the electron density and atom density respectively.

[d]Ar*(4d) lumped excited state includes Ar*(3d, 5s, 5p, 4d).

[e]Since the radiation rate constant from Ar₂*($^3\sum_u$) is 3 orders smaller than Ar₂*($^1\sum_u$), the hν from Ar₂*($^3\sum_u$) are neglected.
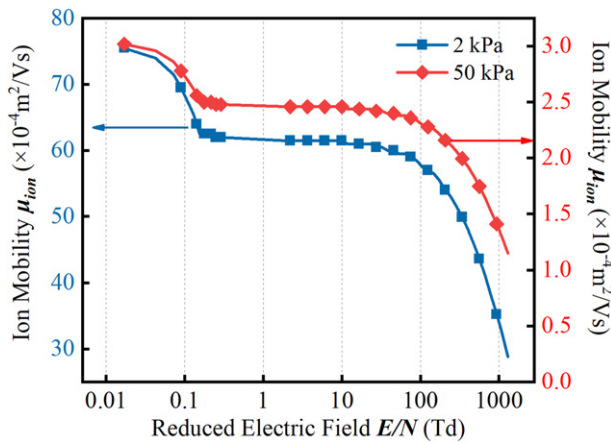
Figure 5. The relationship between ion mobility and reduced electric field at different pressures.

affected by the reduced electric field (*E/N*) and the gas. The nonionic electron-yielding processes (γ_m and γ_p) make a large contribution to the discharge at high pressure. However these processes tend to converge to γ_i at low pressure, which means that the secondary electron emission induced by ion bombardment plays a dominant role [43].

Now regarding photoemission. The photons in pure argon are produced by the excimers Ar₂*, and these excimers are generated by collisions between excited argon Ar* and two ground state argon molecules, which is a three-body reaction, as listed in reaction (8) and (9) in table 1. Most reaction rates increase linearly with gas density *N*, but 3 body reaction rates increase quadratically with *N*. Therefore they are getting more dominant with growing *N*. To sum up, these two mechanism,

ion-induced secondary electrons emission and photoemission, scale oppositely to each other with pressure. If pressure i.e. *N* increases, more photons will be produced but at the same time the drift velocity of ions decreases. Inversely, if pressure decreases, the drift velocity of ions increases but the production rate of photons decreases. In this paper, we focus on the extreme cases of low/high pressure and one will find that the production of new electrons will be dominated by exactly one of these two mechanism. For intermediate pressures, the dynamic behavior would be a mix of the two but that we will not cover that here.

The distinct behavior of the discharge in the two pressure regimes can be understood by investigating the mechanisms that dominate the generation of secondary electrons from the dielectric surface. Two main mechanisms are identified, photoemission or emission by ion bombardment.

It is worth noting that the electron collisional losses for metastable atoms and the step-ionization are very important processes in gas discharge [44]. However, the dominant ionization mechanism at low and high pressure is focused on in this paper, and the discussions indicate that the ion-induced secondary electron emission dominates the ionization propagation and brings about the formation of distinct discharge channels at 2 kPa, and at 50 kPa the photoemission is considered to be chiefly responsible for the ionization evolution and some filaments are evenly distributed through the microcavity. Therefore, in this paper, we mainly take the reactions related to the production of ions and photons, indicated by reactions (1, 3, 5, 7, 9, 10, 11 and 12). Electron collisional losses for metastable atoms are also involved as indicated by reactions (3, 4, 5, 6 and 7). In addition, the step-ionization has been included in this work as indicated by the reactions (2 and 3)

in table 1. The photoemission from Ar (1s4) has not been considered in this paper and previous works [45, 46] have verified that the photoemission in argon primarily comes from the radiation of Ar_2^*.

4. Implementation and solution of a PIC-MCC model for the discharges

4.1. Brief description of the PIC-MCC model

We simulate the discharges in two dimensions using a particle-in-cell model with Monte-Carlo collisions (PIC-MCC) for the electrons. The code is based on the implementation described by Teunissen *et al* [47]. In the PIC-MCC model the electrons are described by super-particles that are accelerated by an electric field and scatter stochastically with gas molecules. The motion and location of electrons is always treated in 3D, but only two spatial coordinates are considered when converting the particles to a density. One super-particle can represent a variable number of electrons, controlled by a weight. The weight is a variable, since particles are adaptively merged or split in order to reduce the computational complexity associated with a large number of particles. Furthermore, the minimum weight of a particle gives a typical length scale of uniformity in the third (neglected) dimension. For our simulations we have taken a minimum particle weight of 10^5, which corresponds to a typical length scale of 10 μm.

Since the velocity of atoms and molecules at room temperature are pretty slow, and due to low ion mobility at high pressure, ions only move 1/10 of cavity depth under 10 V μm^{-1} condition at tens of nanoseconds which is the characteristic duration time of discharge, important species that are produced by electron scattering, such as ions or the argon excimer state (Ar_2^*), are incorporated as an immobile density. One exception to this is the treatment of argon ions in low pressures. In that regime the ion movement plays an important dynamic role, namely the liberation of free electrons from the dielectric surface by ion bombardment.

Hence in that regime the ions are described by super-particles which do not collide and move with a drift velocity $v_{drift} = \mu_{ion} E$. Once an Ar^+ particle reaches the dielectric surface it has a probability $\gamma_{ion} = 0.1$ to liberate an electron. The space and time discretization parameters in this paper can be found in the appendix.

4.2. Implementation of the dielectric boundary

Furthermore, the decay of Ar_2^* produces photons with energies that allow for the liberation of an electron from a dielectric surface. Since photon absorption by argon is negligible, we can assume that photons propagate until they hit the dielectric (or leave through the sides of the domain). Thus, after a photon is produced it is emitted isotropically and we calculate where it reaches the boundary of the domain. If the photon collides with the surface then it has a probability $\gamma_{photon} = 0.05$ to liberate an electron. Note that in this work the photons are considered individually, i.e. as particles with unitary weight. However they are produced by the radiative decay of Ar_2^*, which is given by a density. To account for the discrete and stochastic
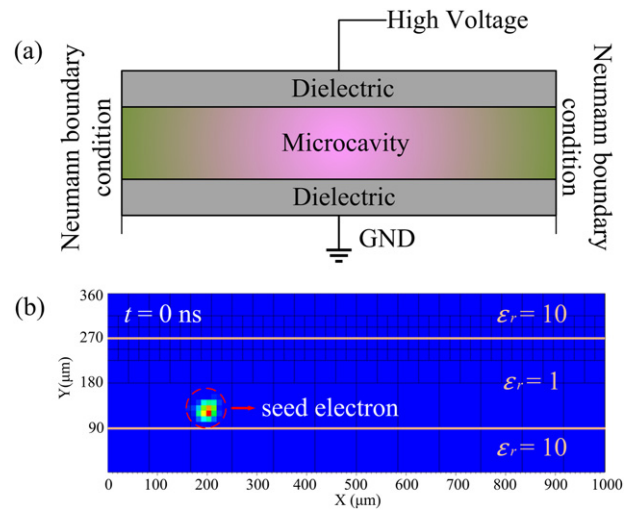

Figure 6. The simulation model adopted in the article. (a) The configuration of model and the boundary condition, (b) the implementation of seed electron and the set of relative permittivity at three domains.

nature of photon emission, the number of photons produced per timestep Δt in a cell with dimensions Δx is drawn from a Poisson distribution with mean λ.

$$\lambda = k n_{Ar_2^*} * \Delta x^3 \Delta t \qquad (2)$$

with $k = 2.4 \times 10^8$ s^{-1} given by reference [36], the reaction constant associated with the radiative decay of the density of argon excimer $n_{Ar_2^*}$. Furthermore, to avoid negative densities no photons are produced if $n_{Ar_2^*}$ is lower than a threshold density which corresponds to one particle per cell.

In this research the electrodes are covered with a dielectric material that can have a surface charge. This introduces a jump condition in the electric field at the interface between the dielectric and the gas. Our numerical treatment of these jump conditions is based on the ghost fluid method (GFM) [48]. Furthermore, whenever a particle (electron or, in the low-pressure regime, ion) collides with the dielectric we consider that the particle attaches to the dielectric in the form of an immobile surface charge. Our implementation of the GFM allows for adaptive mesh refinement along the surface, which means that it can be used in conjunction with the Poisson solvers of the Afivo framework.

As shown in figure 6(a), high voltage 2 kV is applied to the electrode above the upper dielectric layer and the electrode below the lower dielectric layer is grounded. Here, we use Dirichlet boundary conditions on the upper and lower sides of the model to fix the electric potential, and Neumann boundary conditions on the lateral boundaries that means electric field is parallel. Considering that the microdischarge ignites in the corner of microcavity, the seed electrons in the simulation model are set at the left side of cavity to trigger the microdischarge as shown in figure 6(b). The propagation of microplasma will start here. The relative permittivity of dielectric and gas are set to 10 and 1, respectively. Besides, the existence of charge distribution at the boundary of plasma region and dielectric region may lead to the uncertainty of numerical calculation.
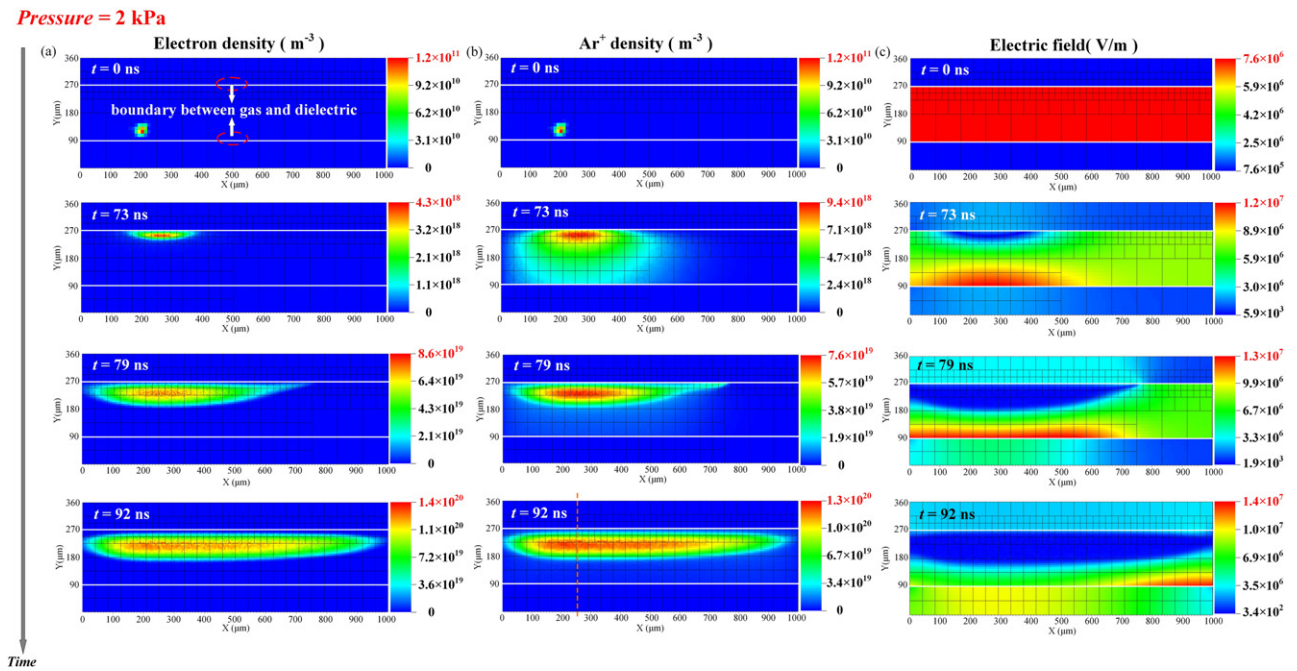
Figure 7. Simulation results at low pressure 2 kPa.

In order to ensure the stability of the numerical value, we use grid refinement to deal with the red line region near 270 μm in figure 6(b).

5. Simulations results and discussions

The evolution of the micro-DBD discharge is now simulated at different pressures, including the temporal-spatial distributions of pivotal particles (e, Ar$^+$) and electric field, and the effect of the pressure-dependent secondary electrons emission on the micro-DBD discharge is studied.

5.1. Simulations results at low pressure 2 kPa

Figure 7 displays the temporal-spatial distributions of electron density, Ar$^+$ density and electric field at a low pressure of 2 kPa which indicates the evolution of electron generation up to 92 ns, that is accurately matching the discharge duration time in the experiment. At $t = 0$ ns, we show the initial electron seed near the dielectric layer at the ground electrode. As the discharge progresses, the peak electron density remains at $y = \sim 250$ μm, however we observe that the discharge gradually expands to the right side of the microcavity. At the end of the simulation, at 92 ns, the whole microcavity is filled with microplasma and the maximum electron density can reach to $\sim 1.4 \times 10^{20}$ m^{-3}. Note that the microdischarge evolves parallely to the dielectric surface, which means that the ionization wave travels along the direction perpendicular to the applied electric field. From the simulation results, the ion density near the lower dielectric surface can reach to $\sim 10^{18}$ m^{-3}, indicating that abundant ions bombard on the dielectric surface to induce secondary electron emission, and the density of these new electrons can reach to $\sim 10^{17}$ m^{-3}. From the temporal-spatial distribution of electric field, before

the generation of microdischarge, the electric field is evenly distributed in space, and with the progress of discharge the electric field begins to be distorted that in the discharged region the electric field decrease due to the shield effect of charged particles. In addition, to identify the effects of secondary emission coefficient of ion impact on the ionization process, simulations with different secondary emission coefficient induced by ions $\gamma_i = 0.05, 0.1, 0.2$ have been carried out as shown in figure 8. The results indicate that the variation of γ_i only influence the initial time of microdischarge and does not change the evolution morphologies of microplasma at low and high pressures.

5.2. Simulations results at high pressure 50 kPa

The temporal-spatial distributions of electron density, Ar$^+$ density and electric field at high pressure 50 kPa is displayed in figure 9, the distribution of electron density does not exhibit the propagation phenomenon that appear in the discharge at low pressure. Instead, due to the non-local nature of photoemission, filamentary discharges are found randomly throughout the domain. As can be seen at $t = 9.8$ ns, a filament is generated on the right side of the domain. As the filaments propagate they connect and finally fill the entire discharge volume. The maximum electron density is $\sim 6.3 \times 10^{20}$ m^{-3}. At high pressure 50 kPa, the mobility of the ions are significantly low, and therefore ions almost never collide with the dielectric in the timescales considered as shown at $t = 16.4$ ns, where the ion density at the lower dielectric layer is $\sim 10^{11}$ m^{-3}. The evolution of electric field at high pressure corresponds to that of the charged particles, as shown by the right column in figure 9 at $t = 9.8$ ns, the shielding of electric field occurs simultaneously at different positions of microcavity. Noting that the inceptive discharge duration time is ~ 16 ns presented
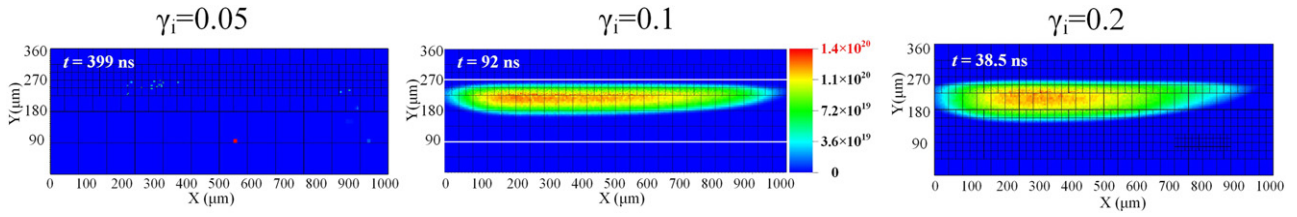
Figure 8. The simulation results of electron density for different secondary electrons emission coefficients by ions at 2 kPa.
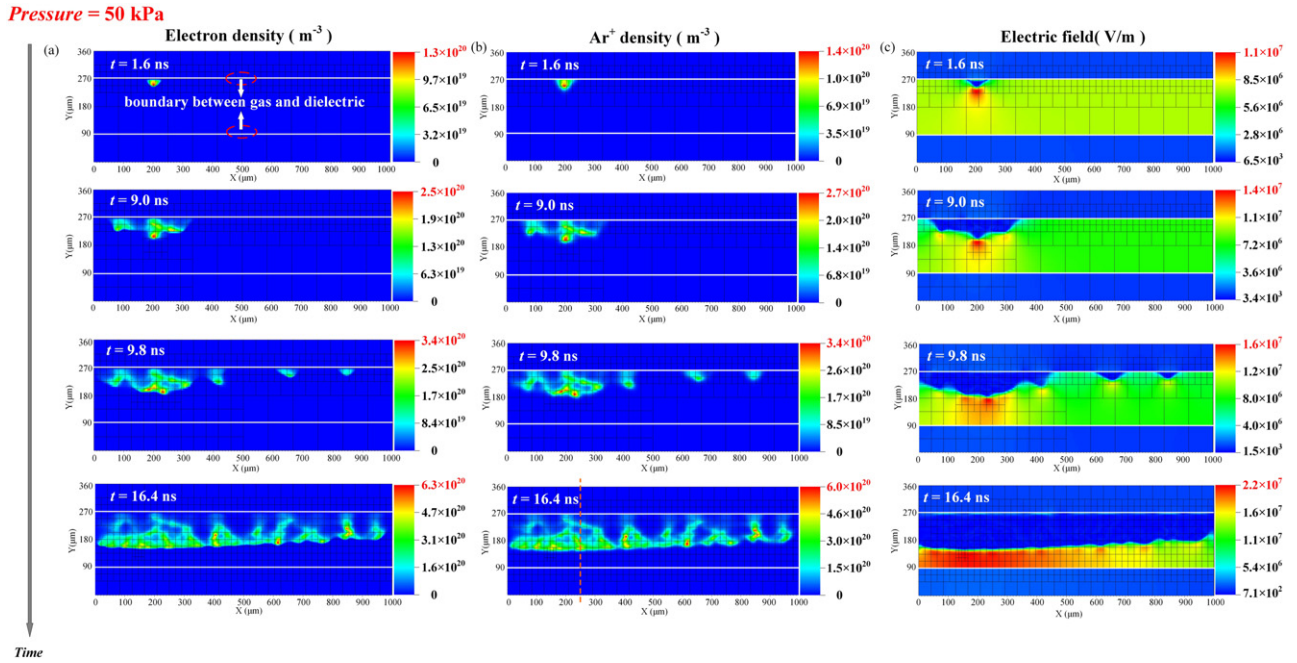

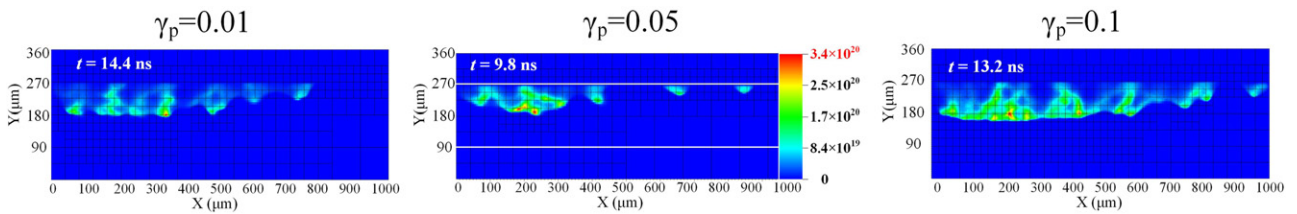**Figure 9.** Simulation results at high pressure 50 kPa.

Figure 10. The simulation results of electron density for different secondary electrons emission coefficients by photons at 50 kPa.

in the simulation results, which is also matching the time scale occurred in the experiment. Similarly to the simulation at 2 kPa, to identify the effects of secondary emission coefficient of photon impact on the ionization process, the simulations with different secondary emission coefficient induced by photons $\gamma_p = 0.01, 0.05, 0.1$ have been carried out as shown in figure 10. The results also illustrate that the variation of the secondary electron emission coefficient of photon impact will not change the ionization mechanism at 50 kPa.

5.3. Discussions

In order to show the distribution of Ar$^+$ density at lower dielectric surface more accurately at 2 kPa and 50 kPa, the spatial distribution of Ar$^+$ density at $X = 250\ \mu$m, i.e. the location indicated by the orange dotted lines shown in figures 7 and

9, is graphed as demonstrated in figure 11. The blue and red solid lines represent the logarithm of Ar$^+$ density at $t = 92$ ns of low pressure 2 kPa and at $t = 16.4$ ns of high pressure 50 kPa separately. Here we select 92 ns and 16.4 ns because the discharge evolution is completed at these moments. At $Y = 90\ \mu$m the lower dielectric surface, the Ar$^+$ density can reach to $\sim 10^{18}$ m^{-3} at 2 kPa, but it can only be $\sim 10^{11}$ m^{-3} at 50 kPa which is 7 orders of magnitude less than that at 2 kPa. The ion bombardment on the dielectric will liberate enough secondary electrons to sustain the subsequent discharge at low pressure 2 kPa.

The initial time of second streamer is determined by the excimer density of Ar$_2^*$, and here an estimated density of excimer Ar$_2^* \sim 10^{16}$ m^{-3} is given to judge if the photoemission could be excited effectively, and the photoemission will be
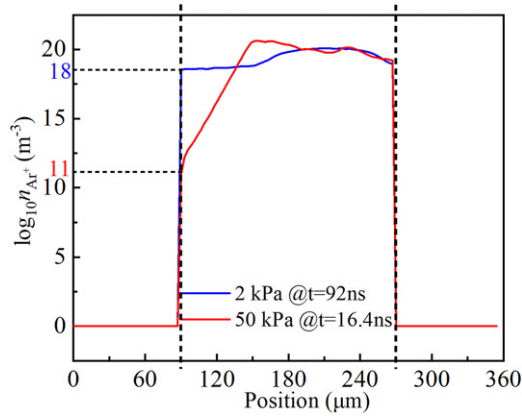
Figure 11. The line profile of spatial distribution of Ar$^+$ at $X = 250\ \mu$m at 2 kPa and 50 kPa.

Figure 12. The temporal distribution of maximal Ar$_2^*$ density at different pressures. (a) Low pressure 2 kPa, (b) high pressure 50 kPa.

stimulated when Ar$_2^*$ density reaches $\sim 10^{16}$ m^{-3}. The critical Ar$_2^*$ density is estimated from the reaction (12) listed in table 1. Here, take 1 as the number of photon generated by the radiation of Ar$_2^*$, therefore the photon density n_{photon} $= 1/V_{\text{cell}}$. From reaction (12), the rate coefficient R is 2.4 $\times 10^8$ s^{-1} and according to the relation $n_{\text{photon}} = n_{\text{Ar2*}} \times R \times \tau$, the threshold Ar$_2^*$ density 10^{16} m^{-3} can be estimated. In the current model, the photoemission probability is fixed at 0.05. The peak Ar$_2^*$ ($^1\sum_u$) densities varied with times at different pressures are captured to investigate the possibility of photoemission, as shown in figure 12. It can be seen that the maximal density of Ar$_2^*$ ($^1\sum_u$) is $\sim 1.3 \times 10^{17}$ m^{-3} at 50 kPa and this is larger than the threshold density 10^{16} m^{-3} to lead the photoemission, which means the photons radiated from the excimer Ar$_2^*$ ($^1\sum_u$) at high pressure are the dominant process to trigger subsequent ionization. Nevertheless, the maximal density of Ar$_2^*$ ($^1\sum_u$) is $\sim 3.7 \times 10^{13}$ m^{-3} at 2 kPa and this is lower than the estimated value. In addition, considering that the Ar$^+$ density bombarding on the lower dielectric surface can reach 10^{18} m^{-3}, the secondary electron emission induced by ions is the dominant process to sustain the subsequent discharge.

In order to explore the evolution of electric field at low pressure 2 kPa and high pressure 50 kPa, the spatial distribution of electric field E at $Y = 250\ \mu$m is plotted in figure 13, in which figure 10(a) displays the spatial distribution of electric field at 2 kPa and figure 13(b) illustrates the spatial distribution of electric field at 50 kPa. From figure 13(a), at the initial discharge stage, the discharge region mainly concentrated on the left side of microcavity as indicated by dip of the red line that the profile of electric field at $t = 73$ ns, and with the progress of discharge, the discharged area gradually expands to the right side of the microcavity as shown by the blue line of electric field at $t = 79$ ns. Finally, at $t = 92$ ns, the whole microcavity space is ignited as indicated by the green line. At high pressure 50 kPa, the initial discharge point appears at $t = 1.6$ ns as indicated by the dip of black line and however, when the discharge reaches to $t = 9.8$ ns, there are three discharged region throughout the microcavity and this is presented by the three dips of blue line in figure 13(b).
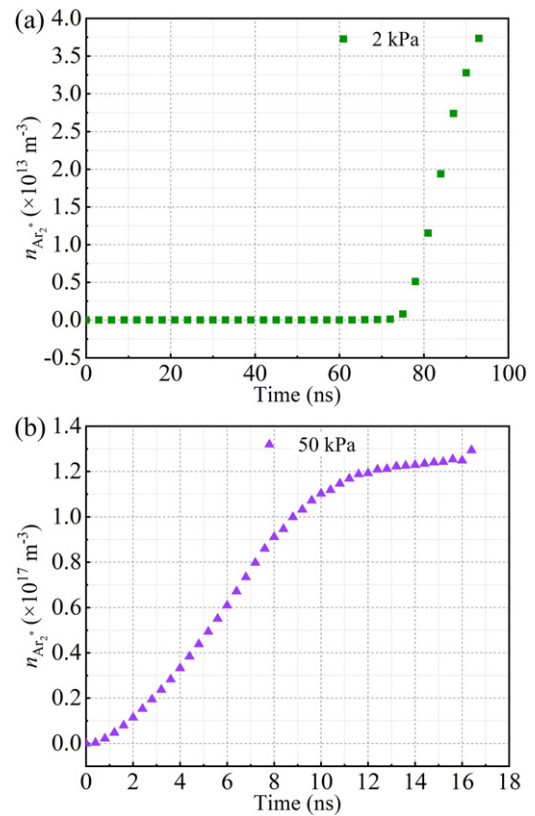
At high pressures, the photoemission process dominates the discharge. It is worthy to note that the screening effect of plasma is observed near the upper dielectric, however in the lower dielectric layer, the electric field seems to be enhanced and this is the opposite of screening effect, as indicated by the spatial-temporal distributions of electric field in figures 7(c) and 9(c). The enhancement of electric field near the lower dielectric layer is speculated to be induced by the accumulation of positive particles in the space, because the mobility of positive particles is much lower than that of the electrons. With the extension of simulation time, the positive particles could drift to the lower dielectric layer and the screening effect of plasma will fill the entire microcavity space.

At low pressures, ion bombardment of the dielectric surface dominates the liberation of secondary electrons. The drift of positive ions is constrained by the electric field distribution, and then the ion-induced secondary electron emission is affected by the random background ionization, which caused the formation of individual discharge channels. The branching and confluence of plasma waves has been reported in reference [29], in which the interactions between adjacent microbranches are presumed to be responsible for the stable branch array. Moreover, the number density N of gas atoms is not large enough to cause the photoemission which can be inferred from the reactions (8) and (11). The three-body reactions are pressure-dependent and thus at lower pressure these reactions slowdown, which means that there are fewer photons be created. At high pressure, the mobility of positive
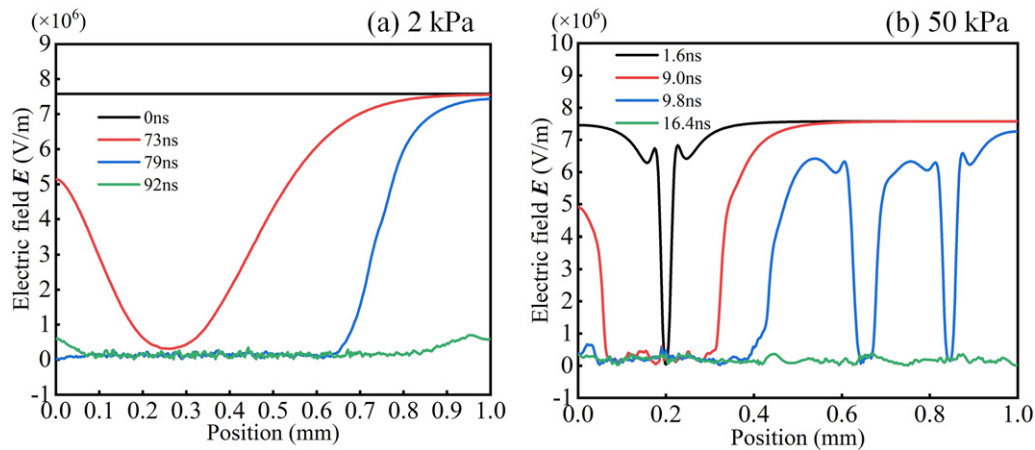
Figure 13. Distribution of electric field at different pressures. (a) At low pressure 2 kPa, (b) at high pressure 50 kPa.

ions decrease with pressure which indicates that most of Ar^+ cannot bombard on the dielectric layer to achieve effective secondary electron emission, and by this time, the photoemission process dominates the continuous discharge and ionization wave propagation. Take the following three aspects into account: (a) the UV photons are emitted radiatively (isotropic), (b) the photon absorption length by the gas is assumed to be very large, (c) the motion of photons is not restrained by electric field, more discrete discharge points would be generated at high pressure.

For low pressure 2 kPa, there are practically few photons and the secondary electrons emission induced by ions dominates the production of new electrons. But for high pressure 50 kPa, lots of photoemission can be generated and the drift velocity of ions is so low that few ions could bombard on the dielectric layer to release new electrons. Ion motion can only generate electrons locally, and thus the discharge can only grow locally at low pressures. For photoemission, a photon can travel across the microcavity and thus new electrons are created non-locally and individual filaments will incept across the whole cavity at high pressures.

Take the calculation cost of PIC-MCC model and the requirements on computer into account, the work presented here is only to simulate the inceptive discharge process, and in the future investigations, we will combine the PIC-MCC model with fluid model to balance the calculation accuracy and cost, to realize the 3D simulation of discharge evolution after the emergence of the ionization wave. In addition, the discharge time in our experiments is not match to the simulations. Actually, the 'voltage rise time' of plasma in experiments must be considered and the discharge cannot emerged immediately once the external power is applied. However, the electric field in simulation can be applied instantaneously. These questions will be discussed in our future works.

6. Summary

Two distinct inceptive micro-discharge modes at low and high pressure have been observed and analysed. For low pressure

we observe a local discharge which propagates transversely, whereas in high pressures a non-locally filamentary discharge is generated. The formation mechanism of the phenomenon is analysed and attributed to different secondary electron emission mechanisms which are dominate at different pressures. At low pressure ion bombardment is dominant, but at high pressures photoemission is the prominent process to produce new electrons. In addition, a 2D PIC-MCC model is used to simulate the time evolution of the species that determine the dynamic behaviour (e, Ar^+, Ar_2^*) and electric field, which showed the influence of the pressure dependence on the two discharge regimes. The simulation results indicate that at low pressure 2 kPa, Ar^+ can bombard on the dielectric layer surface to induce enough secondary electron emission to support self-sustain discharge. Nevertheless, there are not enough excimer Ar_2^* to release photoelectrons effectively at low pressure, which means that the ion-induced secondary electron emission dominates the discharge process. At high pressure 50 kPa, the decrease of ion drift velocity and density causes a negligible amount of ions to reach the dielectric and does not lead to significant secondary electron emission, however, the density of excimer Ar_2^* can reach to $\sim 10^{17}$ m^{-3} to trigger effective photoelectron emission to sustain subsequent discharge.

Data availability statement

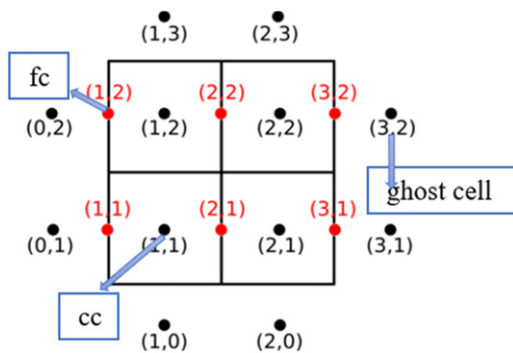All data that support the findings of this study are included within the article (and any supplementary files).

Figure 14. Example of mesh of 2 × 2 cells.

Appendix A

Time and space integration in the simulations.

A.1. Time discretization parameters

Here, the Courant–Friedrichs–Lewy (CFL) condition is used to estimate the time restrictions to electrons and ions separately, as shown in the following.

$$\frac{\Delta t \sum |v_i|}{\Delta x} < 0.5,$$

where v_i is the component of velocity, Δx is the mesh distance. It is founded that when CFL is 0.5, the calculation accuracy and cost could be well balanced.

In addition, the time step is also limited by the dielectric relaxation time, in the code maximum and minimum time step have been set as 10^{-10} s and 10^{-14} s separately.

A.2. Space discretization parameters

Based on the explicit finite volume method, variable storage is carried out in the center (cc) and face center (fc) of the cell, as displayed in the following figure 14.

Afivo framework provides the adaptive refinement of meshes, and the criterion of refinement is based on the local electric field, as indicated in the following.

$$\Delta x < \frac{C_0}{\alpha(E)},$$

where α is ionization coefficient dependent on electric field, C_0 is constant. The reason for using this criterion is that $1/\alpha$ is a typical length scale for ionization, so that the space charge layers of a discharge will have a width of a few times $1/\alpha$.

ORCID iDs

Yaogong Wang https://orcid.org/0000-0002-1244-9361
Xiaoqin Ma https://orcid.org/0000-0002-8514-7903
Dennis Bouwman https://orcid.org/0000-0002-9590-4816
Ute Ebert https://orcid.org/0000-0003-3891-6869

References

[1] Ouyang J, Li B, He F and Dai D 2018 *Plasma Sci. Technol.* **20** 103002
[2] Wang Y, Zhang X, Liu L, Zhou X, Liu C and Zhang Q 2018 *Phys. Plasmas* **25** 043506
[3] Wang Y, Ni J H, Zhong S, Zhang X, Liang Z, Liu C, Park S J and Eden J G 2016 *J. Phys. D: Appl. Phys.* **49** 415206
[4] Liu H, Yi P, Lu W, Zeng X, Xu L, Wang X, Zhu Q and Xiong Q 2017 *IEEE Trans. Radiat. Plasma Med. Sci.* **1** 460
[5] Sheng C L, Chien J Y and Keh C L 2016 *J. Vac. Sci. Technol.* B **34** 02G106
[6] Yang R, Sazonov A and Karanassios V 2016 Flexible, self-powered, visible-light detector characterized using a battery-operated, 3D-printed microplasma operated as a light source *Conf. on IEEE SENSORS* (Orlando, FL: USA) pp 1–3
[7] Becker K H, Schoenbach K H and Eden J G 2006 *J. Phys. D: Appl. Phys.* **39** R55
[8] Bose A, Narakathu B, Bazuin B and Atashbar M 2018 *Proceedings* 2
[9] Lin L and Wang Q 2015 *Plasma Chem. Plasma Process.* **35** 925
[10] Kong M G, Kroesen G, Morfill G E, Nosenko T, Shimizu T, van Dijk and Zimmermann J L 2009 *New J. Phys.* **11** 115012
[11] Becker K H, Kersten H, Hopwood J and Lopez J L 2010 *Eur. Phys. J.* D **60** 437
[12] Lee H W, Park G Y, Seo Y S, Im Y H, Shim S B and Lee H J 2011 *J. Phys. D: Appl. Phys.* **44** 053001
[13] Moselhy M, Shi W, Stark R H and Schoenbach K H 2001 *Appl. Phys. Lett.* **79** 1240
[14] Zhu X M, Walsh J L, Chen W C and Pu Y K 2012 *J. Phys. D: Appl. Phys.* **45** 295201
[15] Tachibana K 2006 *IEEE J. Trans. Elec. Electron. Eng.* **1** 145
[16] Wang Y G, Ma X Q, Hu L, Zhou X, Wang Z X and Zhang X N 2019 *Phys. Plasmas* **26** 112103
[17] Cho J H, Yang H J, Park S J and Eden J G 2019 *J. Phys. D: Appl. Phys.* **52** 375202
[18] Cho J H, Park S J and Eden J G 2012 *Appl. Phys. Lett.* **101** 253508
[19] Boettner H, Waskoenig J, O'Connell D, Kim T L, Tchertchian P A, Winter J and Schulz-von der Gathen V 2010 *J. Phys. D: Appl. Phys.* **43** 124010
[20] Liu X M, Song Y H, Jiang W and Jia W Z 2018 *Chin. Phys. Lett.* **35** 045202
[21] Akishev Y, Aponin G, Balakirev A, Grushin M, Karalnik V, Petryakov A and Trushkin N 2011 *Plasma Sources Sci. Technol.* **20** 024005
[22] Seo J H and Eden J G 2006 *J. Appl. Phys.* **100** 026107
[23] Lee H J, Park S J and Eden J G 2012 *J. Phys. D: Appl. Phys.* **45** 405201
[24] Wollny W *et al* 2011 *Appl. Phys. Lett.* **99** 141504
[25] Wollny W, Hemke H, Gebhardt G, Brinkmann B R and Mussenbrock M 2011 *IEEE Trans. Plasma Sci.* **39** 2684
[26] Wang D, Wang L and Zheng Y 2018 *J. Appl. Phys.* **124** 203301
[27] Sharma S, Kumar N, Hussain S and Sharma R P 2017 *Laser Part. Beams* **35** 10–8
[28] Brauer I, Punset C, Purwins H G and Boeuf J P 1999 *J. Appl. Phys.* **85** 7569
[29] Wang Y, Zhou X, Ma X, Zhang X, Liu C, Liu D, Park S-J and Eden J 2019 *Plasma Sources Sci. Technol.* **28** 09LT01
[30] Hayashi M 2003 *Science* (Toki: National Institute for Fusion)
[31] Hayashi M 2018 www.lxcat.net Hayashi database (www.lxcat.net, retrieved on 14 August 2018)
[32] Yanguas-Gil Y-G, Cotrino C and Alves L 2005 *J. Phys. D: Appl. Phys.* **38** 1588
[33] Hyman H A 1979 *Phys. Rev.* A **20** 855
[34] Treshchalov A B and Lissovskii A A 2010 *Quantum Electron.* **40** 234

[35] Neeser S, Kunz T and Langhoff H 1997 *J. Phys. D: Appl. Phys.* **30** 1489

[36] Dyatko N A *et al* 2008 *J. Phys. D: Appl. Phys.* **41** 99

[37] Tian P 2018 *PhD Thesis* University of Michigan

[38] Treshchalov A B and Lissovski A A 2009 *J. Phys. D: Appl. Phys.* **42** 245203

[39] Treshchalov A B and Lissovski A A 2006 *Atomic & Molecular Pulsed Lasers VI* **6263** 62630H–1

[40] Madson J M and Oskam H J 1967 *Phys. Lett.* A **25** 407

[41] Phelps A V 1991 *J. Phys. Chem. Ref. Data* **20** 557

[42] Grubert G K, Loffhagen D and Uhrlandt D 2005 *Proc. FEMLAB Conf.* p 6

[43] Yoshinaga T and Akashi H 2014 *IEEE J. Trans. Elec. Electron. Eng.* **9** 459

[44] Carbone E, van Veldhuizen E, Kroesen G and Sadeghi N 2015 *J. Phys. D: Appl. Phys.* **48** 425201

[45] Amsler C, Boccone V, Büchler A, Chandrasekharan R, Regenfus C and Rochet J 2008 *JINST* **3** P02001

[46] Oka T, Kogoma M, Imamura M, Arai S and Watanabe T 1979 *J. Chem. Phys.* **70** 3384

[47] Teunissen J and Ebert U 2016 *Plasma Sources Sci. Technol.* **25** 044005

[48] Liu X-D, Fedkiw R P and Kang M 2000 *J. Comput. Phys.* **160** 151